7.1 Introduction

Different combination of organic linkers and SBU of metal clusters give rise to a hybrid material with many interesting properties, like high specific surface area, porous periodic framework, easy processibility, high thermal and mechanical stability [1]. The hybrid material, MOF has already shown its versatility and applicability in numerous fields: from gas adsorption to energy storage, from heterogeneous catalysis to biomedicine etc [2],[3]. Depending on the topology of the SBUs the structure and morphology of the MOFs are determined. One of such MOFs is UiO-66 which exhibits high stability towards adverse chemical environment and high temperature. An ideal crystalline UiO-66 MOF is believed to have high coordination number of Zr- SBU connected to 12 terephthalic (BDC) linkers [4]. However, several investigations in the past have shown that treatment after synthesis, or even during synthesis may cause defects in UiO-66 by leaving out 3 to 4 linkers from each cluster, leading to missing cluster defects, vacancy defects etc. [5]. It was found that defects have interesting consequences over the crystalline materials, like the simplest example of forming *p*-*n* junction using doped semiconductors fall into the basic of defect engineering. Similarly, defect engineering in MOFs can reveal hidden active sites and broaden the scope of their potential applications. A careful removal of some of the metal nodes or linkers, which is frequently done in defect engineering of MOFs, results in a variety of different MOF features, such as a larger accessible internal area, increased porosity, and more catalytic and adsorption sites, all of which have a significant positive impact on performance in the relevant applications [6],[7]. Previously, a simple one pot hydrothermal synthesis has created a UiO-66 with missing linker defect which was further used for phosphomolybdic acid (HPMo) encapsulation to attain catalysis of oxidative desulfurization [8]. There is also evidence of modifying UiO-66 using other MOF like MOF-5 to obtain a missing-linker defect for toluene adsorption [9].

Swift heavy ion (SHI) irradiation is a process through which a target material is exposed to high energetic ion beams to induce imperfections, and structural changes in the material. When materials are bombarded with energetic ions, a wide range of defect states are produced, changing the material's physicochemical characteristics, including its macrostructure, optical properties, and electrical transport characteristics [10]. This is,

because, the incident ion's mass, irradiation energy, and fluence all significantly influence the alterations. The irradiation may generate ionisation or excitation, as well as potential atomic displacement from their locations in the materials' lattice [11]. SHI irradiation effect on different MOFs has been worked out in the recent years, for instance nickel-based nanorods of MOF (NRs-Ni_3HHTP_2 MOF, $HHTP_2$- *hexahudroxytriphenylene*) were irradiated with C^{12+} ions in the fluence range, 10^{11} -10^{12} ion/cm^2 [12]. Observable changes as regards, structural, spectroscopic, morphological, optical, and field effect transistor (FET) have been witnessed. They concluded that the material property changes caused by SHI irradiation were useful for improving field-effect transistor (FET) qualities and sensing properties. R. Dutta and group has irradiated Ni-BTC MOF composite of PVDF polymer with 100 MeV O^{7+} to investigate the ionic liquid (IL) uptake capacity of MOF composite [13]. Irradiation effectively enhanced the intake of IL % as SHI enlarged the size of micropores by creating missing linker defect. SHI irradiation has been used in enhancing electrochemical properties of polymer-based nanocomposites in various works [13]–[16]. One significant work was modification of surface properties using 100 MeV O^{7+} ion irradiation on MoS_2-rGO/PPy nanotube nanocomposite electrodes. The group used the irradiated electrode for supercapacitor application and found improvement in the properties like specific capacitance, energy density, cyclic stability etc. at certain fluence. In another work Polyaniline (PAni) nanofibers grown inside the interlayer galleries of montmorillonite (MMT) was irradiated with 100 MeV Si^{9+} ions. They investigated the electrochemical properties of the nanocomposite as a polymer electrolyte which displayed highest conductivity up to 8.4×10^{-2} S cm^{-1} at a fluence of $1x10^{12}$ ions/ cm^2.

The present work discusses solvothermally derived UiO-66 MOFs followed by irradiation with 60 MeV N^{5+}ions in the fluence range, 5 x 10^{10}- 1 x 10^{12} ions/cm^2. After studying structural, vibrational, morphological, and electrical properties the electrodes of irradiated MOFs have been modified with biomolecules namely, mouse immunoglobulin G (IgG) to evaluate the electrochemical performance in detecting the antigen goat anti mouse IgG. Electrochemical sensing technique has been employed for unirradiated and irradiated systems to further investigate the analyte detection quantitatively, and on a comparative basis.

7.2 SHI irradiation experiment on UiO-66 MOF fabricated on ITO coated glass

The UiO-66 power was fabricated onto ITO glass of size 1 x 1.5 cm via slurry coating method as described in Chapter 2. Electrodes of UiO-66 have also been made to measure the electrical property after irradiation. The swift heavy ion irradiation on UiO-66 films and electrodes were carried out at Inter University Accelerator Centre (IUAC), New Delhi, India, using material science beam line. The films were irradiated at normal incidence with 60 MeV N^{5+} ions considering fluences of 5 x 10^{10}, 1 x 10^{11}, 5 x 10^{11}, 1 x 10^{12} ions/cm^2 under a vacuum of 10^{-6} Torr. The fluences (φ) were determined from the relation-

$$T = \frac{\varphi \times A \times n \times e}{I} \qquad (7.1)$$

using current (I) equal to 1 pnA, exposed area i.e., 1 x 1 cm^2, electronic state(n) = 5+ and charge e =1.9 x 10^{-19} Coulomb [17]. During energetic ion bombardment energy transfer to the target occurs through two processes nuclear energy loss (S_n) and electronic energy loss (S_e). The electronic energy loss mechanism predominates in SHI in the MeV range, where a highly confined region around the ion passage is excited by the ion beam. A standard software on Stopping and Range of ions in Matter (SRIM) was used to calculate the projectile range, nuclear energy loss and electronic energy loss. The projected range for N^{5+} ion was found to be 81.93 μm which is higher than the thickness of the UiO-66 films (40-60 μm). The S_e and S_n values are calculated to be ~50.9 eV/Å and 0.0295 eV/Å, respectively.

7.3 Structural and morphological features

7.3.1 X-ray diffraction studies

X-ray diffraction data of pristine UiO-66 MOF and the samples irradiated with 60 MeV N^{5+}ions are shown in Fig. 7.1 (a). Apparently, the diffraction peaks at, 2θ=7.1, 8.21, 11.72, 25.3° corresponded to (111), (002), (022), (115) planes of commonly known face-centered cubic lattice of UiO-66 [18]. It can be observed from the Fig. 7.1(b) the intensity and the peak positions of the peak corresponded to plane (111) and (002) which tend to altered after irradiating with varied fluences. A reduction in intensity of the subsequent peaks suggests the overall decrease in crystallinity of the MOF structure, as evident by the values

of the crystallinity index mentioned in Table 7.1. The decrease in crystallinity is an indication of degradation of crystalline phase as an impact of SHI irradiation. It was seen that the diffraction peaks in the samples exposed to 5x 10^{10} and 5x 10^{11} ions/cm^2 have shifted towards lower Bragg's angle. During the first two fluences shifting of the peaks was believed to be due to the thermal expansion that would take place in the crystalline motif upon exposure to high energy ion beams [19]. The UiO-66 irradiated with 1x10^{12} ions/cm^2 showed a noticeable degradation in the intensity of the diffraction peaks accompanied by peak shifting towards higher angle by 0.2 degree. The development of compressive strain in the structure was expected at this fluence which resulted in the peak shifting towards the higher angle and consequently, the reduction in *d*-spacing. (Fig. 7.1 (b)). Average crystallite size was calculated using Debye Scherrer equation considering the peak of (111) crystallographic plane. For the first fluence the average crystallite size remains unchanged but at a fluence of 5x 10^{11} ions cm^{-2}, crystallite size seems increased. This increase in crystallite size can be attributed to the irradiation-induced heating and coalescence of smaller crystallites or grains into larger ones [20]. Wherein, at the higher fluence of 1x 10^{12} ions cm^{-2}, peak widening in the XRD spectra is observed, which suggests that the crystallite size of UiO-66 MOF has been reduced. A possible explanation for this decrease in crystallite size is strain-induced grain fragmentation during SHI irradiation [21]. These results implying the prevalent occurrence of defects in the irradiated samples of UiO-66.

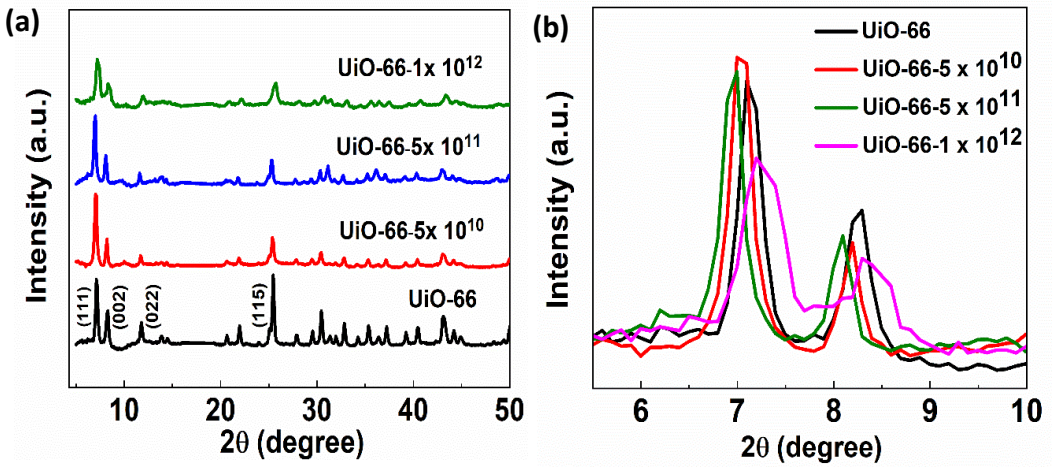

Fig. 7.1. (a) XRD pattern of UiO-66 MOF and samples irradiated with different fluence, (b) XRD peak shift after irradiation.

Table 7.1. FWHM, average crystallite size, microstrain, and crystallinity as determined from the XRD pattern of pristine and irradiated UiO-66 at different fluences.

Sample	FWHM (β)	Crystallite size (D) (nm)	Microstrain (ϵ) x 10^{-3}	Crystallinity %
UiO-66	0.2758	28.8	1.19	63
UiO-66-5 x 10 [10]	0.2752	28.9	1.19	46.3
UiO-66-5 x 10 [11]	0.2642	33.9	1.01	49
UiO-66-1x 10 [12]	0.4946	16.16	2.13	37.4

7.3.2 Fourier-transformed IR spectroscopy (FTIR)

FTIR was performed at room temperature in the wavenumber range of 400 -3000 cm^{-1}. The main features exist in the range 400- 2000 cm^{-1} and that 3150 cm^{-1} essentially characterize a band due to O-H stretching of water molecules or solvent residues present in the sample. The organic linker present in the structure acts as a major light absorber in the FTIR spectra of UiO-66 as shown in Fig. 7.2. The carboxylate group of linker forms dimer of HCOOH through H-bonds giving rise to centre of symmetry. While the synthesis of UiO-66 monocarboxylic acid is used as modulator to slow down the crystallization process in order to obtain better crystallinity. If missing linker defects are present in the clusters of UiO-66, COO^- group of modulators can cap the defect sites by binding with Zr^{4+} sites through unidentate coordinate bonds. From the earlier studies it was observed that open Zr sites neighbouring to the COO^- bonded sites are filled by water molecules through H-bonding which stabilizes the COO^- groups. The bands above ~ 1600 cm^{-1} are assigned to the vibration of COO^- groups due to the monocarboxylic acid [22]. Here in this study the use of benzoic acid during the synthesis can lead to such a configuration which can lead to the emergence of a C=O stretching mode at 1662 cm^{-1}. Studies suggested that on heating at a temperature below 150^o C can remove the water molecules bonded at the defect sites, indicated by the diminished peak between ~1600-1700 cm^{-1} [22]. The signature peak got disappeared in the irradiated samples. This may be due to the excessive heat caused by high energy radiations, resulting in the removal of water molecules. In UiO-66 the presence of COO- groups of BDC linker causes the stretching vibration in C=O bonds dictated by the absorption peak at ~1399 cm^{-1}. The peaks at 1579 cm^{-1} and 1507 cm^{-1} are attributed to symmetric and asymmetric stretching modes of C=C of BDC

linker. These peaks are seen to be consistent in the irradiated samples. The modes at lower frequencies~ (748 cm^{-1}, 557 cm^{-1}) are wagging vibrations of C-H and C-C bending mixed with Zr-O bonds and that ~664 cm^{-1} and 447 cm^{-1} are contributions from stretching modes of μ3-O and μ3-OH [6].The samples that were exposed to fluences 5 x 10^{11} and 1x 10^{12} ions cm^{-2} exhibited lower band intensities at about 1018 cm^{-1} and 748 cm^{-1} in comparison to their unirradiated counterpart. This decrease in intensity is possibly due to the removal of C-H bonds present in the benzene ring of the linker due to effect of heavy ion irradiation. Since DMF and benzoic acids are used during the synthesis of UiO-66 there can be competition between the formate ions and COO^- groups to cap the defects sites for charge neutralizing. These formate capping could have removed during the irradiation process revealing the missing linker defect sites. This can be the possible reason behind the quenching of vibrational modes in the lower frequency region [23].

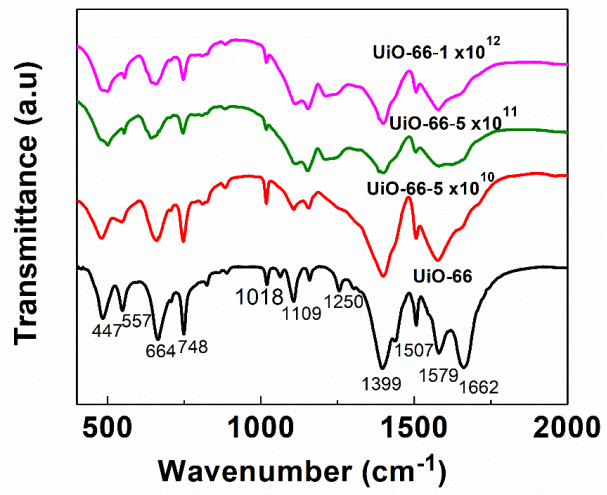

Fig. 7.2. FTIR Spectra of UiO-66 and samples irradiated with different fluence.

7.3.3 Raman spectroscopy

Because UiO-66 has a hugely complex structure comprising plentiful atoms, there can be multitude of near adjacent IR or Raman active modes. Vibrational motion of different atoms present in the MOF's organic linker mostly comprise the modes in the 600–1700 cm^{-1} region (Fig. 7.3). The symmetric stretching modes of the carboxylate ligand, O-C-O, are responsible for the strong peak at ~ 1608 cm^{-1}. At a wavenumber of 1430 cm^{-1}, there

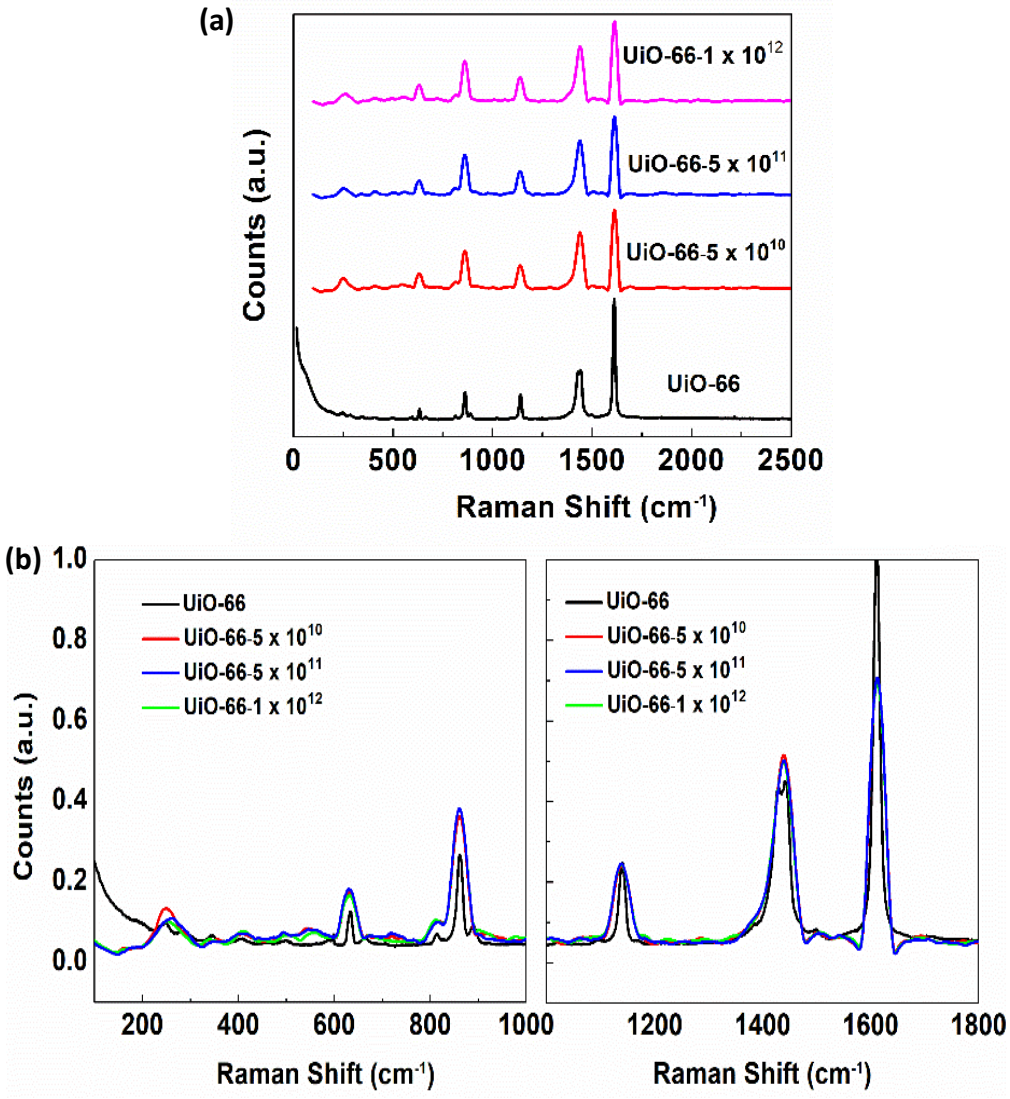

Fig. 7.3. (a) Raman spectra of unirradiated and irradiated UiO-66 with different fluence (b) Magnified spectra in the range of 100-400 cm^{-1}.

exist an in-plane vibration of C=C-H bending with C=C stretching. The peaks at ~ 1140 cm^{-1} and 869 cm^{-1}, respectively, are caused by aromatic ring breathing paired with C=C-H stretching and C=C(OO) symmetric stretching [24]. The bands from 600 to 1700 cm^{-1} are nearly identical to the parent UiO-66 based on our observations in the irradiated samples. This demonstrates that topology of post-irradiated MOF was unaffected. But a lower intensity in the peak at 1608 cm^{-1} in the irradiated films has been observed indicating the reduction of the scattering centres as a result of missing linkers. On the other hand, the intensity of the peaks increased in the Raman modes of 869 cm-^{1} and 626 cm^{-1}. This variation in intensity can be ascribed as the deformation in the benzene ring of terephthalic

acid. A shoulder peak arises at 809 cm^{-1} due to the motion of carboxylate group in charge stabilizing benzoate molecule. After ion irradiation effect, deformation has occurred in the benzene ring of benzoate giving rise to high intensity Raman bands in the radiation induced samples [25]. The bands are feeble in the fingerprint region due to motion of metal cluster coordinated with different oxo and hydroxyl group present in the organic linker. The peaks at 344, 285 and 246 cm^{-1} are the result of linker to metal cluster bonds twisting, torsioning, and bending in-plane and out-of-plane, respectively [23]. Changes in the peaks around this frequency range can be seen in the irradiate samples. The irradiated samples' peak at 285 cm^{-1} is increased with the appearance of new shoulder peaks that are blue-shifted. These modifications imply that there has been some stretching of the Zr-(OC) bond in the irradiated samples.

7.3.4 Morphological study

The morphology of unirradiated and irradiated UiO-66 at fluences 5 x 10^{10}, 5 x 10^{11} and 1x 10^{12} ion cm^{-2} can be found in Fig. 4 (a). The pristine UiO-66 has collective octahedral particles with spheroid morphology that has an average size ~ 170 nm as analysed from particle size distribution. After irradiation the particle size was seen to get increased gradually with increasing ion fluence (Table 2). During ion fluence of 5 x10^{10} ion cm^{-2} the spheroid trend of particles remained same as the pristine one. At an ion fluence of 5 x10^{11} ion cm^{-2} the shape remained same as the UiO-66 and with a larger size. At the highest fluence, aggregation of particles is seen, giving rise to a bigger size of particle with no uniform shape. The reason behind these results can be assumed due to the grain growth occurring after recrystallization of the particles [20]. When the materials are bombarded with high energy heavy ions, it would transfer sufficient amount of heat to lattice sites to cause the generation of thermal spikes within the material. These thermal spikes can lead to rapid melting and subsequent solidification, facilitating the coalescence of neighbouring grains and the growth of larger grains over time [26].

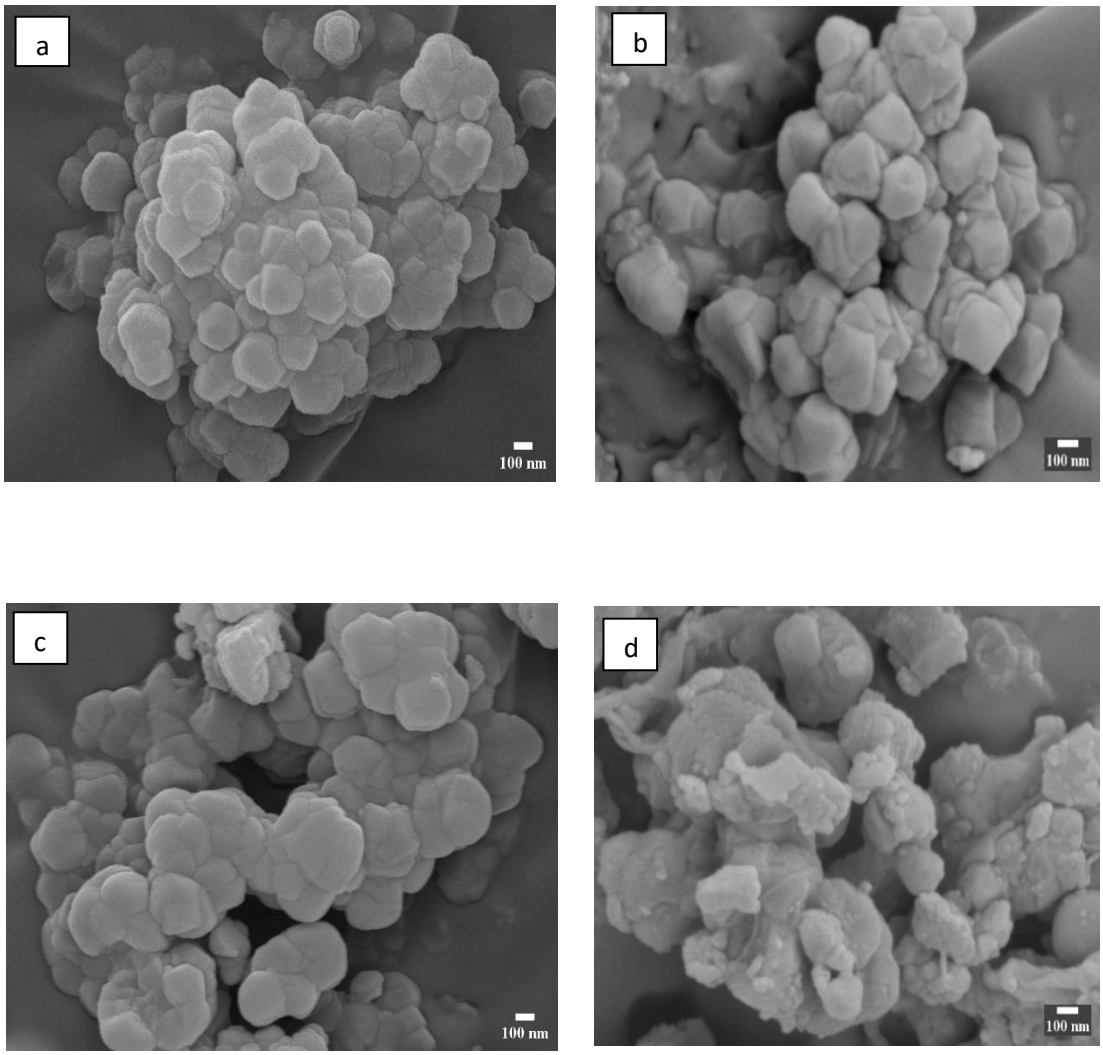

Fig. 7.4. FE-SEM images of (a) UiO-66 at 40 kX and (b) UiO-66 -5 x 10^{10} ions cm^{-2} at 50 kX, (c)) UiO-66-5 x 10^{11} ions cm^{-2} at 40 kX, (d)) UiO-66-1 x 10^{12} ions cm^{-2} at 50 kX.

Table 7.2 Average particle size analysed from FESEM images and conductivity calculated from I-V plots of pristine and irradiated UiO-66

Sample	**Average particle size (nm)**	**Conductivity (S cm^{-1}) X 10^{-9}**
UiO-66	177.89	1.07
UiO-66-5 x 10^{10}	204.61	7.20
UiO-66-5 x 10^{11}	259.29	36.16
UiO-66-1 x 10^{12}	338.29	14.80

7.4 *I-V* characteristics

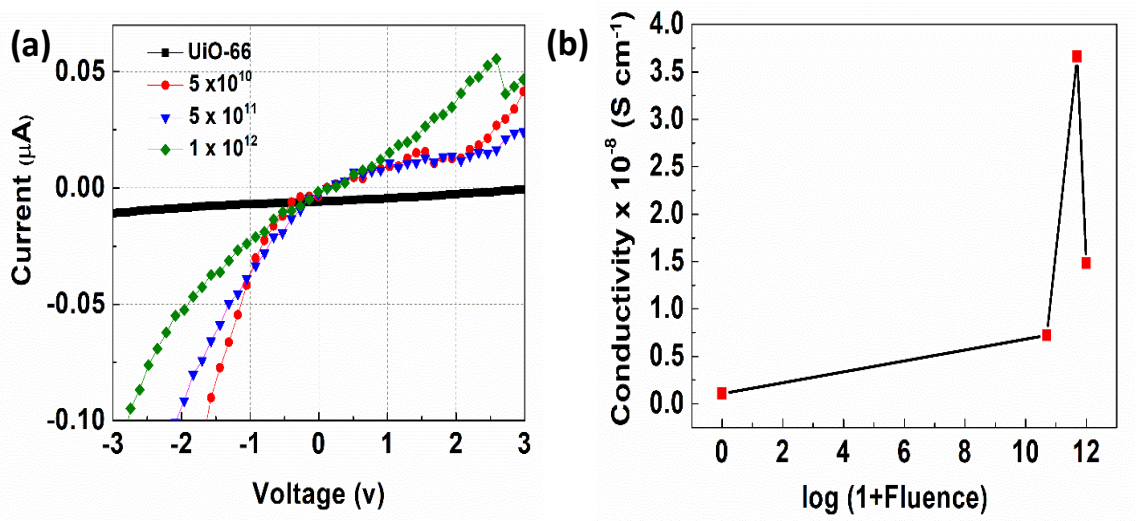

Fig. 7.5. (a) *I-V* characteristics of UiO-66, UiO-66-5 x 10^{10}, UiO-66-5 x 10^{11}, UiO-66-1 x 10^{12} and (b) Conductivity at different fluences.

The samples were studied for electrical transport measurements in a two-probe setup with a source meter in a voltage range of -3V to 3V. Resembling metal-semiconductor rectifying trend, shown in Fig. 7.5. (a), the *I-V* plots signify a non-linear trend in all the irradiated samples. The unirradiated sample has a very low current response in lower nA range with respect to increasing voltage. As irradiation was implicated the current response is seen to be increased in all the cases with different slopes for the linear segment. The conductivity was calculated using the slope of linear part of the *I-V* curves with the formula $\sigma = \left(\mathcal{G}\frac{l}{A}\right)$ where $\mathcal{G}$ is the slope, l is the distance between the probe, A is the area of the pellets. It was found that the value of conductivity linearly increased at first up to the fluence of 5 x 10^{11} ion/cm^2, shown in Fig. 7.5. (b). and at the highest fluence, the conductivity is dropped. In MOFs conductivity is generally low due to the absence of free charge carriers and low energy path for charge transport [27]. The increase in conductivity after irradiation implies to the enhancement in carrier concentration due to delocalization, or enhancement in carrier mobility. The interaction of high energy N^{5+} ions and target atoms of UiO-66 can give rise to electronic excitation and hence increment in carrier density. Also, the SHI irradiation can cause structural rearrangement in the material providing more conductive pathways, leading to an augment in conductivity. However, at the highest fluence, 1 x 10^{12} ion cm^{-2} the conductivity dropped to 9.28 x 10^{-9} S cm^{-2}. The observed decrease in

crystallinity following irradiation at the maximum fluence could potentially be attributed to the introduction of amorphous phases, which could obstruct the charge transport channels.

7.5 Electrochemical performances of irradiated samples

7.5.1 Cyclic Voltammetry and EIS studies

Electrochemical tests were performed in a 3-electrode system with a 5 mM $[Fe(CN)_6]^{3-/4-}$ mixture of 1.0 mM PBS as electrolyte for pure UiO-66 and the irradiated samples. All the materials showed obvious pair of redox peaks in the potential window of -0.2V to 0.6V, at a scan-rate of 20 mV/s. According to Nernst equation for an electrochemically reversible reaction electron transfer between analyte and electrode is smooth which is often considered to have a peak-to-peak separation of (ΔE) 57 mV and $\frac{I_{pc}}{I_{pa}} \cong 1$ [9]. As shown in Fig. 7.6, in all the cases of radiation induced electrodes as well as unirradiated UiO-66 the values of ΔE and $\frac{I_{pc}}{I_{pa}}$ doesn't meet the conditions of Nernst equation as mentioned above (Table 3). This implies sluggish reaction between the analyte and electrode which in turn causes slow electron transfer rate as the reduction potential increases for all the cases. Cyclic Voltammograms shown in Fig. 7.6 depicts that electrode irradiated with $5x10^{10}$ and $5x\ 10^{11}$ ion cm^{-2} have an enhanced response to current in terms of potential change. In case of exposure at highest fluence, the response degrades. There are different factors which can affect the electrochemical performance like electrode material, temperature, scan-rate, pH of the electrolyte, concentration of the analytes etc. While these conditions are kept same and only electrode material is altered, the enhancement or reduction in the performance is obviously due to the pretreatment on the electrode material by ion fluence. When the electrodes were bombarded with energetic ions changes occurred in the crystal structure of the MOFs as observed in the XRD studies. The creation of dislocation, vacancies in the structure can influence the effective surface area of the electrode which in turn enhances the current density by providing more sites for the electrochemical reaction. Raman analysis have shown that there are defects occurred in the metal cluster node of UiO-66 that can be attributed to O vacancy. These sites may catalyse the reaction

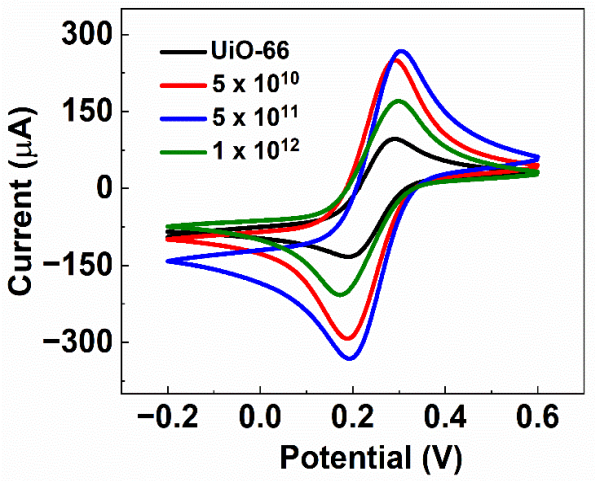

Fig. 7.6. CV of UiO-66, UiO-66-5 x 10^{10}, UiO-66-5x10^{11}, UiO-66-1x10^{12} systems.

between the analyte and electrode, leading to the enhancement in current density. However, in the highest fluence the current density decreased which can be implied by decrease in crystallinity in this particular fluence. This structural disorder can reduce the well-defined pathways for reactant and product diffusion to the electrode surface which results in slower reaction kinetics and hence reduction in current response.

Table. 7.3 Peak separation and redox peak current determined from cyclic voltammetry of pristine and irradiated UiO-66 electrodes

Electrode	**Peak Separation ΔE (V)**	**Peak Current (Oxd^n) I_{pc} (μA)**	**Peak Current (Red^n) I_{pa} (μA)**
UiO-66	0.125	173.7	- 210.9
UiO-66-5 x 10^{10}	0.113	266.3	-331.2
UiO-66-5 x 10^{11}	0.1	251.8	-295.1
UiO-66-1 x 10^{12}	0.091	95.7	-134

The electrochemical impedance spectroscopy (EIS) results are in accordance with the CV test as the charge transfer impedances of irradiated samples varied with ion fluence. The Nyquist plot of pristine and irradiated samples in the frequency range of 0.1- 10^6 Hz can be found in Fig. 7.7 (a). The semicircle in the higher frequency region arises due to the impedance occurred during charge transfer and electrical double layer (EDL) capacitor at the electrode-electrolyte interface. The plots were fitted to the Randles equivalent circuit

according to which R_s is the series resistance, R_{ct} is the charge-transfer resistance, CPE is the capacitor formed at higher frequency at the interface. At the lower frequency range, a spike line has occurred making an angle almost equal to 45° which arises due to the transport of ions or molecules to or from the electrode surface. This linear part represents the Warburg impedance (*W*) of the system. The semicircle is larger in case of fluence $1x10^{12}$ ions cm^{-2}, illustrating the greater difficulties the electrodes encountered in charge transfer. The analysed value of R_{ct} (Table 7.4) of this electrode is larger than the other electrodes. In fact, electrodes with fluence $5\ x10^{10}$ and $5\ x10^{11}$ ions cm^{-2} have similar R_{ct} values which would imply the better electron transfer kinetics after irradiation. The Warburg impedance of the electrodes irradiated with fluence $5\ x10^{10}$ and $5\ x10^{11}$ ions cm^{-2} is nearly similar to that of UiO-66 which means diffusion-controlled processes of charge transfer kinetics at the electrode surfaces has not varied after irradiation.

Table.7.4 EIS parameters obtained from the equivalent circuit

Sample	R_s (Ω)	R_{ct} (Ω)	*W* (Ω $s^{-1/2}$)	CPE (F)	C_2 (F)
UiO-66	40.96	82.34	$3.31\ x10^{-3}$	$4.11\ x10^{-6}$	$31.7\ x10^{-3}$
UiO-66-5 x 10^{10}	49.38	101.1	$4.64\ x10^{-3}$	$4.64\ x10^{-6}$	$930.5\ x10^{-3}$
UiO-66-5 x 10^{11}	40.34	102.1	$3.51x10^{-3}$	$4.377\ x10^{-6}$	$50.79\ x10^{-3}$
UiO-66-1 x 10^{12}	41.48	198.6	$1.329\ x10^{-3}$	$62.67\ x10^{-3}$	$67.03\ x10^{-3}$

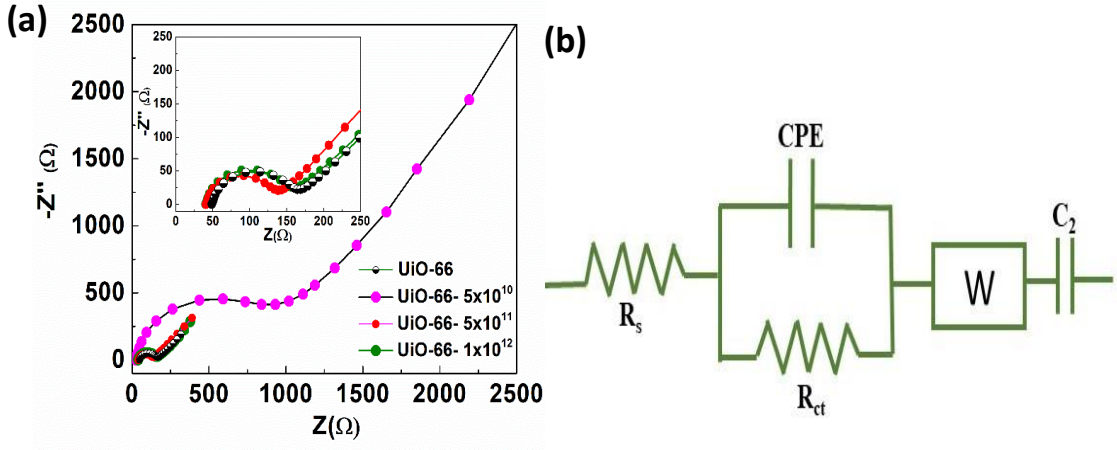

Fig. 7.7. (a) EIS of UiO-66, UiO-66-5 x 10^{10}, UiO-66-5x10^{11}, UiO-66-1x10^{12} systems. The equivalent circuit for Nyquist plots of UiO-66 and irradiated UiO-66 is shown in (b).

On the other hand, the electrode irradiated at a fluence of 1 x 10^{12}ions/cm^2 has a slightly lower Warburg impedance, which may be due to the larger density of defect that occurred in the crystal structure at this particular fluence.

7.5.2 Scan rate varying CV

To analyse the electroactive surface area of the modified electrodes with ion irradiation the CV has been measured at different scan-rate from 10 mV/s to 100 mV/s. Prior to that response the experiment was performed for UiO-66 electrodes, as shown in Fig. 7.6 (a). The anodic peak current (I_{ap}) and cathodic peak current (I_{cp}) increased linearly with the square root of scan rate (Fig. 7.6 (b)) as depicted by the linear regression coefficient, 0.9906 and 0.9886. This plot fits to the Randles Sevcik equation [28]-

$$I_p = 0.446nFAC^o \left(\frac{nFvD_o}{RT}\right)^{1/2} \quad (7.2)$$

Where A is the electroactive surface area, $D_o$is the diffusion constant of analytes, C^o is the concentration of the analyte, F is Faraday's constant, n is the number of electrons taking part in the reaction. This means that the electron transfer reactions are essentially governed by diffusion-controlled mechanisms. By substituting the slope of I_p vs. $v^{1/2}$ plot in equation (7.2) and considering D_o as 6 x 10^{-6} cm^2/s, the electroactive surface area for UiO-66 electrode was calculated to be 1.31 cm$^{2.}$ Similar experiment was performed for the electrodes irradiated with different fluences. By analysing the redox peaks of scan-rate varying CV data for those electrodes it was found that the electroactive surface area of electrode modified with 5x10^{10} and 5x 10^{11} ions cm^{-2} fluences have larger values as compared to the unirradiated UiO-66 electrode (Fig 7.8 (c), (d), (e), (f)). The A values are 1.913 cm^2 and 2.05 cm^2 for UiO-66-5x10^{10} and UiO-66-5x10^{11}, respectively. On the other hand, the A reduced in the electrode UiO-66-1x10^{12} clearly explains the drop in electrochemical performance of the electrode (Fig. 7.8 (g), (h)).

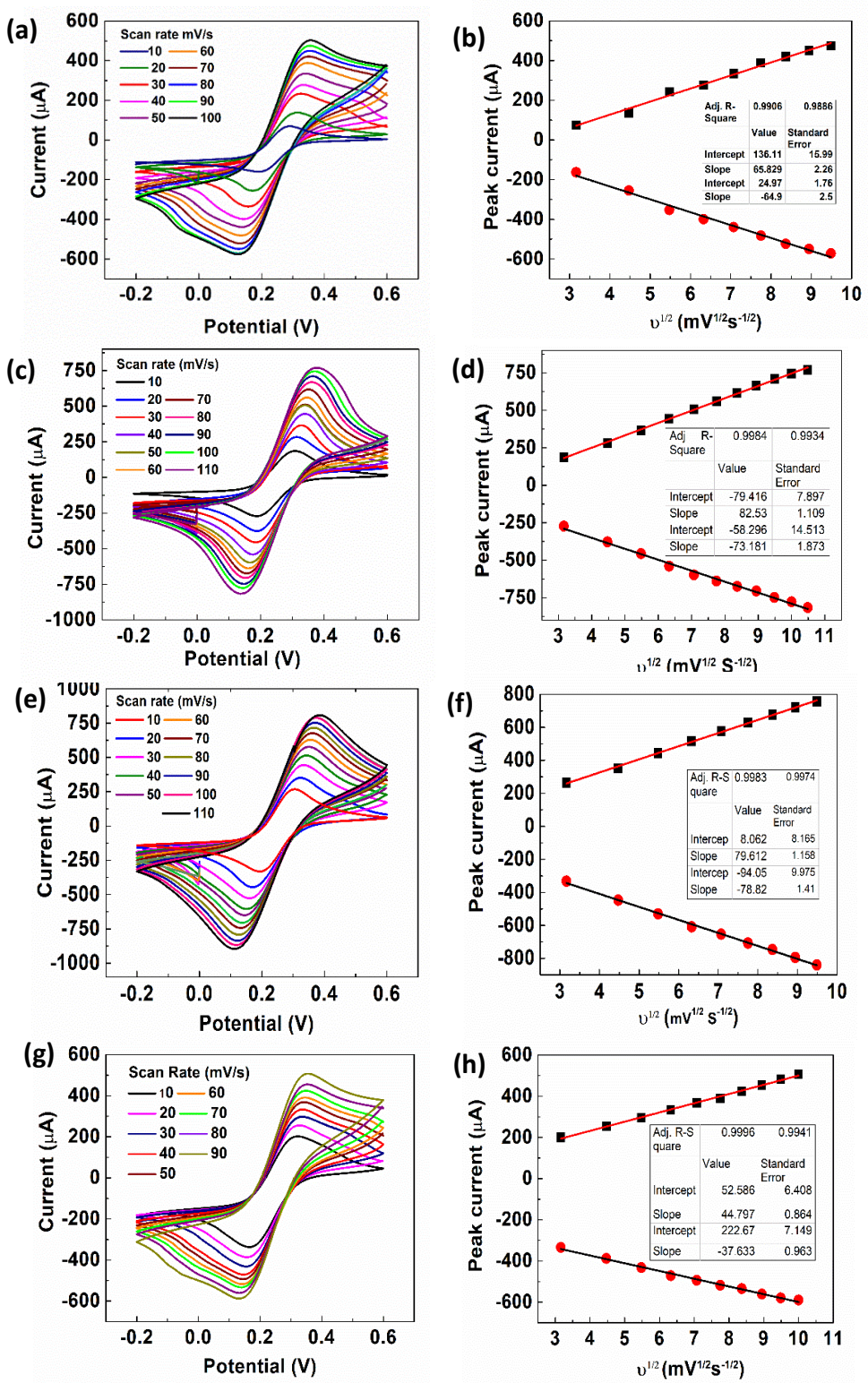

Fig. 7.8. Scan-rate varying CV and linear plot of square root of scan-rate vs. peak current of (a) and (b) UiO-66; (c) and (d) UiO-66-5 x 10^{10}; (e) and (f) UiO-66-5 x 10^{11}; (g) and (h) UiO-66-1 x 10^{12}.

7.6 Modification of the electrodes by immobilizing biomolecule.

The irradiated electrodes were used for the detection of biomolecule anti Goat mouse IgG by immobilizing antibody mouse IgG in it with the help of cross-linking agent glutaraldehyde (Gu). After adding every layer of modifiers to the electrodes irradiated with N^{5+} ions, CV and EIS responses were monitored to confirm the immobilization of the biomolecules. Because the cross-linking agent Gu reacts with a variety of functional groups, including the hydroxyl group found in UiO-66 coordinated to Zr-nodes, it binds to the MOF's surface providing the desired sites for biomolecule immobilization. This results in reduction of redox peak current (I_p) and enhancement in carrier-transfer resistance as linking of Gu potentially hinders the charge transfer between the electrode and electrolyte. Since the amino group in mouse IgG had an affinity for the aldehyde group, Gu served as a binder to attach biomolecules to the electrode surface. As a result, I_p reduces again as the biomolecules creates a barrier in diffusion of electroactive species. For an accurate binding of analyte to the antibody unreacted aldehyde sites on the electrode surface are blocked with the help of BSA. Finally, after all the fabrication procedure CV and EIS measurements were performed to observe the biosensor electrodes (Fig. 7.9 (a), (b)). After immobilization of antibody IgG, the CV was performed in 5 mM $[Fe(CN)_6]^{3-/4-}$ mixture of 1.0 mM PBS with a scan rate of 20 mV/s keeping all the experimental condition same as before immobilization. As anticipated, the cyclic voltametric (CV) response decreased by 54%, 62.8%, 51.7%, and 68.86% for UiO-66, UiO-66-5 x 10^{10}, UiO-66-5 x 10^{11}, and UiO-66-1 x 10^{12}, respectively, following the immobilization of the antibody. This reduction is attributed to the blocking of active sites by the immobilized biomolecules, which also increased the charge-transfer resistance, as confirmed by the electrochemical impedance spectroscopy (EIS) analysis. Electrodes modified with radiation fluence 5 x 10^{10} and 5 x 10^{11} ions cm^{-2} has retained their superior performance in comparison to the pristine as well as other fluences. While in the electrode irradiated at 1x 10^{12} the current response decreased to large extent implied through CV and large semicircle of EIS pattern with a R_{ct} value of 5704 Ω (Table 7.5 and Table 7.6). For convenience the mouse IgG immobilised pure UiO-66 and irradiated UiO-66 electrodes were labelled as UiO-Gu-IgG-BSA, UiO-5 x 10^{10}-Gu-IgG-BSA, UiO-5 x 10^{11}-Gu-IgG-BSA and UiO-1 x 10^{12}-Gu-IgG-BSA.

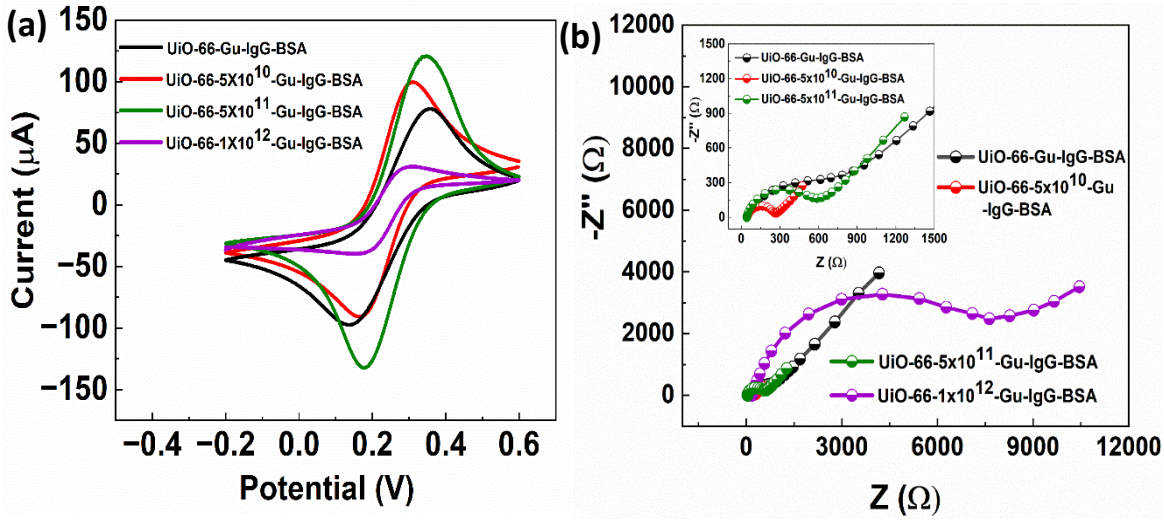

Fig. 7.9. (a) CV and (b) EIS features of UiO-Gu-IgG-BSA, UiO-5 x 10^{10}- Gu-IgG-BSA, UiO-66-5 x 10^{11}- Gu-IgG-BSA, UiO-1 x 10^{12}- Gu-IgG-BSA systems.

Table.7.5. Peak separation and redox peak current determined from cyclic voltammetry of pristine and irradiated UiO-66 electrodes immobilised with mouse IgG

Electrode	**Peak Separation ΔE (V)**	**Peak Current (Oxd^n) I_{pc} (μA)**	**Peak Current (Red^n) I_{pa} (μA)**
UiO- Gu-IgG-BSA	0.215	78.54	-98.09
UiO-5 x 10^{10}- Gu-IgG-BSA	0.13	99.05	-89.74
UiO-5 x 10^{11}- Gu-IgG-BSA	0.16	121.6	133.06
UiO-1 x 10^{12}- Gu-IgG-BSA	0.1	29.80	39.35

Table.7.6. EIS parameters obtained from equivalent circuit of pristine and irradiated UiO-66 electrodes immobilized with mouse IgG

Electrode	**R_s (Ω)**	**R_{ct} (Ω)**	**ω (Ω $s^{-1/2}$)** x10^{-3}	**CPE (F)** x10^{-6}	**C_s (F)** x10^{-3}
UiO- Gu-IgG-BSA	40.7	437.4	261	2.418	5.047
UiO-5 x 10^{10}- Gu-IgG-BSA	41.48	198.6	1.329	2.67	7.030
UiO-5 x 10^{11}- Gu-IgG-BSA	41.70	431.9	1.06	6.112	121.7
UiO-1 x 10^{12}- Gu-IgG-BSA	175.2	5704	0.212	5032	269.9

7.7 Analytical performance mouse IgG immobilized 60 MeV N^{5+} irradiated UiO-66 electrodes

7.7.1 Sensing of Goat anti-mouse IgG

The response of immobilized mouse IgG towards immune-species Goat anti-mouse IgG was studied by performing DPV of fabricated electrodes in redox probe as a supporting electrolyte in a potential window of -0.1V to 0.6 V. The DPV response of UiO-Gu-IgG-BSA on varying concentration of the antigen goat anti mouse IgG from 50 ng/mL to 250 ng/mL can be found in Fig. 7. 10 (a). The black DPV curve is the one taken with no analyte added to the electrolyte. With increasing concentration, the DPV peak height decreases as a result of analyte capture by antibody in its specific sites. When antigen binds to the antibody it hinders the transfer of electrons from the redox probe, $[Fe(CN)_6]^{3-/4-}$ to the electrodes resulting in a low current. The linear plot of change in current (ΔI) and antigen concentration shown in the Fig. 7.10 (b), reveals that the linearity can be found in the concentration range of 50-200 ng/mL. The regression equation of the plot is given by-

$$y = 0.0573\ \mu A ng^{-1} mL\ \times (X) - 0.142;\ R^2 = 0.9989 \qquad (7.3)$$

Using the slope and intercept of the linear plot, LODs were calculated with the formula for LOD = $3 \times S_y/_S$ where S_y is the standard deviation and *s* is the slope of the linear plot [29]. The value of LOD was found to be 7.17 ng mL^{-1} in the linear range of 50-200 ng mL^{-1} with a sensitivity of 0.0573 μA $ng^{-1}mL$.

Similar experiments were repeated for all the irradiated electrodes, the results of which are presented in Fig. 7. 11 (a), (c), (e). The electrode irradiated with fluence 5 x 10^{10} ions cm^{-2} of ions exhibits a better performance than the pristine one while the concentration of the antigen increased. The decrease in peak current is seen to be proportional to concentration. The linear plot (Fig. 7.11 (b), (d), (f)) reveals that the linearity is in the range of 50-300 ng mL^{-1}. This electrode, as anticipated, showed more sensitivity than the unirradiated UiO-66 (Table 7.7). This improvement is in conformity with the findings of the CV and EIS tests. The sensing experiments on UiO-66-5x10^{11}-Gu-IgG-BSA displayed

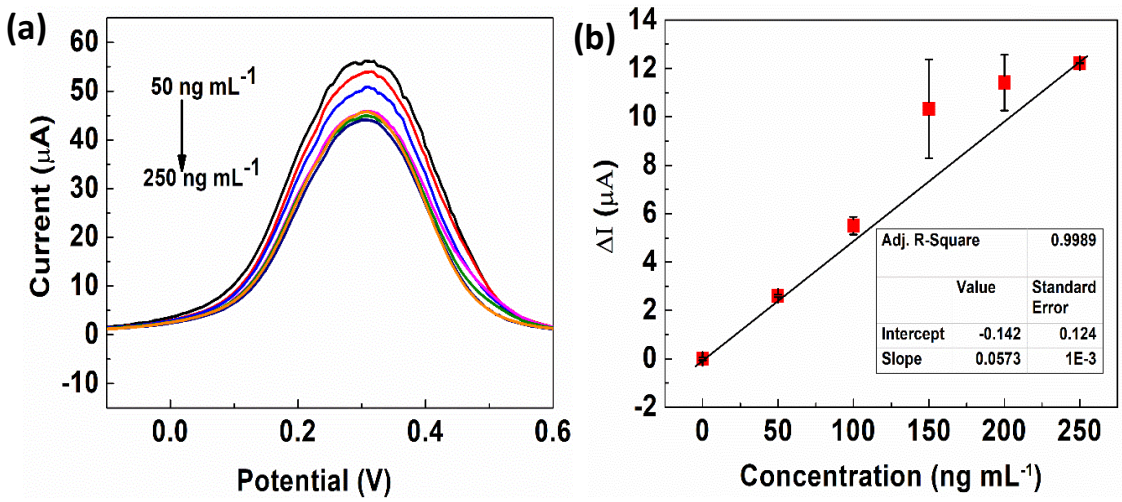

Fig. 7.10. (a) DPV response of UiO-66-Gu-IgG-BSA towards different concentration of goat anti mouse IgG and (b) Linear plot of concentration vs. variation in peak current.

improved results with a higher sensitivity of 0.205 μA ng^{-1} mL^{-1} and lower LOD of 4.13 ng mL^{-1}. This result conferring the results of scan rate varying CV of the electrode that reveals the increased electroactive surface area after irradiation providing ample number of active sites for interaction with the analyte. Again, as for the highest fluence ($1x10^{12}$ ions cm^{-2}) the performance of the electrode degraded. This aspect was also noted in the CV and EIS experiments which may be due to the lattice structure degradation at this fluence.

The calculated values of sensitivity, LOD and linear range are tabulated in the Table 7.7. When these results are compared with the quantitative analysis of UiO-66-Gu-IgG-BSA electrode, the electrodes UiO-66-5 x 10^{10} -Gu-IgG-BSA and UiO-66-5 x 10^{11}-Gu-IgG-BSA displayed better performances in terms of sensitivity, linear range and LOD. On the other hand, UiO-66-$1x10^{12}$-Gu-IgG-BSA electrode displayed a poor performance. Infact, upon irradiation the structural properties of the UiO-66 lattice have been affected as depicted by XRD and vibrational property studies. Due to the possibility of missing linker defects created in the first two fluences the surface area gets enhanced which has revealed in the scan-rate varying CV studies. However, when the fluence was increased

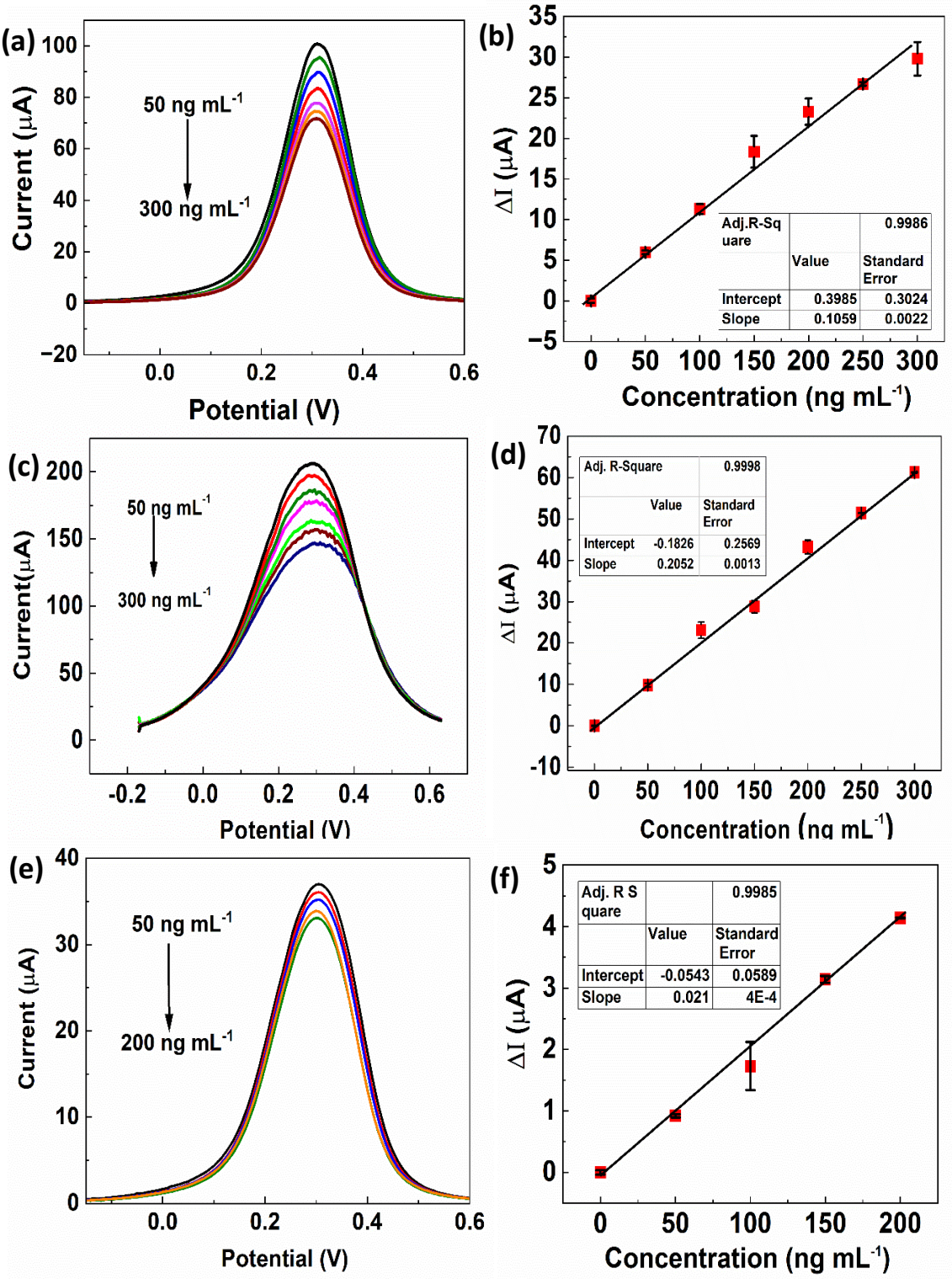

Fig. 7.11. DPV response and calibration plot of (a), (b) UiO-66-5x10^{10}-Gu-IgG-BSA, (c), (d)UiO-66-5x10^{11}-Gu-IgG-BSA, (e), (f) UiO-66-1x10^{12}-Gu-IgG-BSA with varying concentration of goat anti mouse IgG.

to $1x10^{12}$ ions cm^{-2} the density of missing-linker defects may enhance which would result in the degradation of crystallinity of the lattice and agglomeration of particles as obtained from SEM analysis. Clumping of particles together has both positive and negative impact on the electrochemical performances. Negative aspects are like reduction of surface area lowers the number of active sites for analyte interaction and also the analyte preconcentration to the electrolyte which reduces the ion transfer. On the other hand, at some controlled agglomeration in MOF can create pathways for electron transfer which enhances the conductivity of material. This could be the reason of difference in the electrochemical performances of each irradiated sample.

Table 7.7 LOD, sensitivity and linear-range observed when pristine and irradiated UiO-66 electrodes are immobilised with mouse IgG while detecting goat anti mouse IgG

Electrodes	**LOD** **(ng mL^{-1})**	**Sensitivity** **(µA $ng^{-1}mL$)**	**Linear-range** **(ng mL^{-1})**
UiO-66-Gu-IgG-BSA	7.17	0.057	50-200
UiO-66-5 x 10^{10}-Gu-IgG-BSA	9.42	0.1059	50-300
UiO-66-5x 10^{11}-Gu-IgG-BSA	**4.13**	**0.2052**	**50-300**
UiO-66-1 x 10^{12}-Gu-IgG-BSA	9.11	0.021	50-200

7.7.2 Reproducibility of Goat anti-mouse IgG detection Using UiO-66-5 x 10^{11}-Gu-IgG-BSA

Based on structural, morphological, electrical, and electrochemical tests, all of the UiO-66 samples that were exposed to varying fluences of radiation displayed altered attributes. The fluence of 5 x 10^{11} ions cm^{-2} induced structural changes in UiO-66 and, consequently, augmented the conductivity to the highest out of all the fluences. This aspect enhanced the electrochemical performance, and UiO-66-5x10^{11}-Gu-IgG-BSA functioned superior in terms of sensing the bio-analyte with a higher sensitivity and lower LOD. Consequently, the results were replicated in two additional UiO-66 electrodes that were exposed to 5 x 10^{11} ions/cm^2 and immobilized with Gu-IgG-BSA to ensure reproducibility. When the concentration was varied from 50 ng mL^{-1} to 300 ng mL^{-1} the DPV responses declined in the similar manner as the previous electrode as shown in Fig. 7.12 (a) and (c). The LOD

and sensitivity values calculated from the linear plots of concentration vs. peak current are closer to the parameters obtained from the first electrode of UiO-66-5x10^{11}-Gu-IgG-BSA. The sensitivity and LOD findings had an RSD of 3.19% and 8.43%, respectively as tabulated in Table. 7.6 (Fig. 7.12 (b) and (d)). This implies the successive reproducibility of the results ensuring the accuracy of the biosensing electrode.

Table 7.8. Reproduced sensing parameters of UiO-66-5 x 10^{11}-Gu-IgG-BSA

Electrode	LOD (ng mL^{-1})	Sensitivity (µA ng^{-1} mL)
1	4.13	0.2052
2	4.60	0.2005
3	4.89	0.1927
RSD %	8.43	3.19

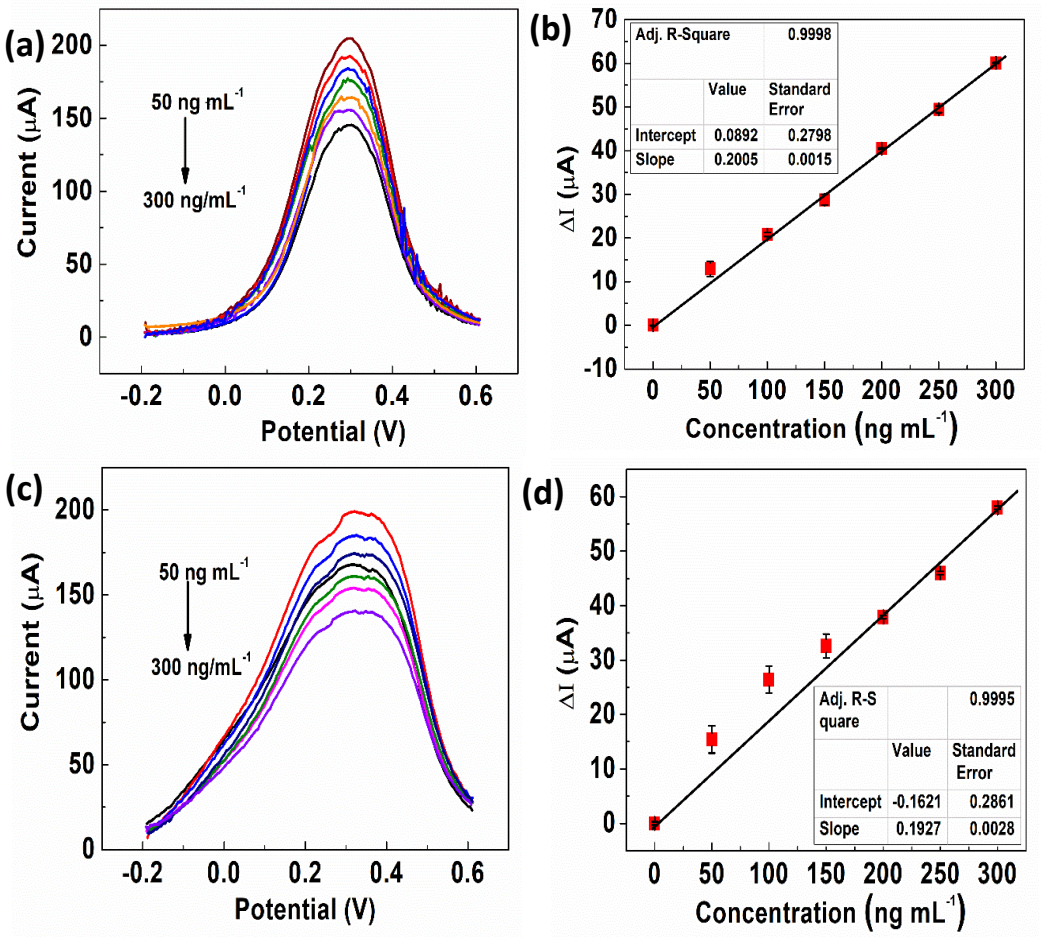

Fig. 7.12. Reproducibility of UiO-66-5 x 10^{11}-Gu-IgG-BSA in sensing Goat anti-mouse IgG with (a) electrode 2, (b)calibration plot of electrode 2, (c) electrode 3, (d) calibration plot of electrode 3.

7.7.3 Selectivity test on UiO-66-5 x 10^{11}-Gu-IgG-BSA for Goat anti-mouse IgG

Moreover, the electrode was tested for its selectivity towards the specific analyte Goat anti-mouse IgG in presence of other interfering analytes like Human IgG and Anti-Aflatoxin B1(AFB1) (Fig. 7.13). The test was performed in 1.5 mL 0.1M PBS mixture with 5 mM $[Fe(CN)_6]^{3-/4-}$ supporting electrolyte with DPV technique. The black DPV curve in Fig. 7.13 is the one acquired without adding the analytes and is referred to as blank. In the first step 150 ng mL^{-1} analyte was added to the electrolyte and the DPV measurement were made which resulted in a reduction of the peak current from the blank. Subsequently 150 ng mL^{-1} Human IgG and Anti AFB1were added to the electrolyte. There is no change in the DPV curve found after the addition of interfering analytes. To verify the phenomenon, the DPV response was measured with 250 ng mL^{-1} of analytes, which resulted in a negligible impact on the DPV pattern.

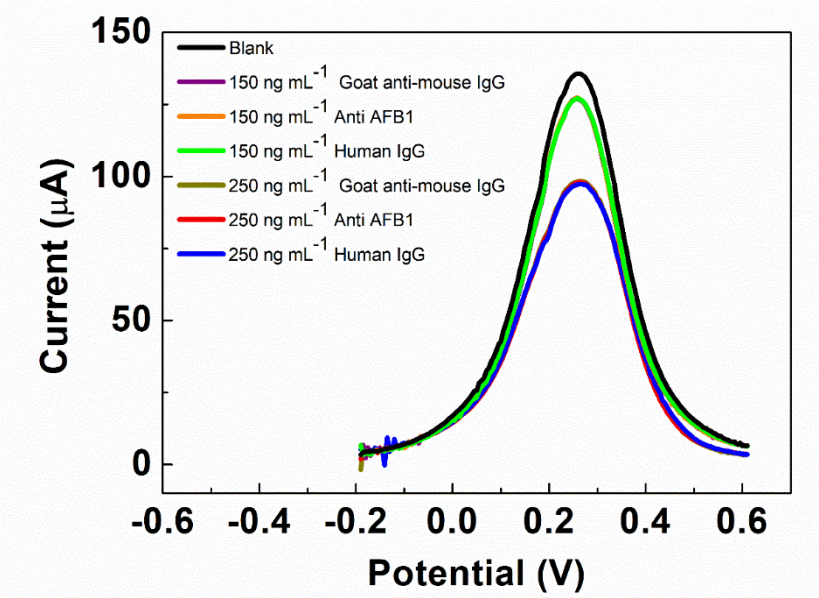

Fig. 7.13. Selectivity test of UiO-66-5 x 10^{11}-Gu-IgG-BSA for Goat anti-mouse IgG.

7.7.4 Stability

The stability aspects of the UiO-66-5x10^{11}-Gu-IgG-BSA electrode were evaluated by performing CV test of 20 cycles at a scan-rate of 20 mV/s in 3 mL electrolyte 0.1M PBS mixture with 5 mM redox probe shown in Fig. 7.14. After 20 cycles, the area under the curve remained approximately same. A slight variation in the redox peaks between the 20th and 1st cycles is observed, with a relative standard deviation (RSD) of 2.6%. This depicts the good electrochemical stability of the electrode for repeatable usage.

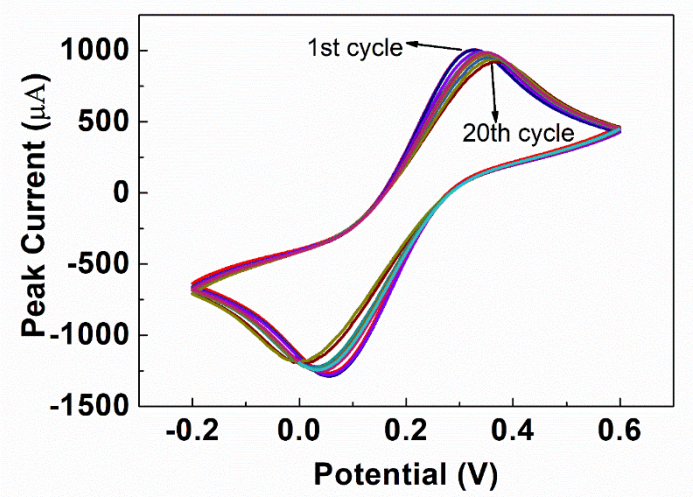

Fig. 7.14. Stability of UiO-66-5 x 10^{11}-Gu-IgG-BSA electrode over cycles 1-20.

7.8 Conclusion

This work demonstrates how 60 MeV N^{5+} ion bombardment on Zr-based MOF UiO-66 electrodes influenced the structural, morphological and electrical and electrochemical properties and consequently the biosensing behaviour. As found from XRD, FTIR and Raman studies structural modification has been witnessed by the irradiation process on UiO-66 MOF. Vibrational spectroscopy studies suggested that irradiation has revealed the missing linker defect sites and created O vacancy in UiO-66 lattice structures. As a result of these structural modifications the conductivity of irradiated UiO-66 got enhanced. In the electrode irradiated with 5x10^{11} ions cm^{-2} the conductivity is increased to 36.1x10^{-9} S cm^{-1} which is the highest amongst pure and all the other irradiated samples. In terms of electrochemical performances also UiO-66-5x10^{11} displayed a superior behaviour as compared with pure and UiO-66 irradiated with other fluences. As expected, while the

irradiated electrodes were employed for the biosensing purpose it has been observed that the electrode irradiated with 5 x 10^{11} ions/cm^2 offers a better sensing activity amongst other irradiated electrodes. Interestingly it has better sensitivity of 0.2052 μA ng^{-1} mL^{-1} with lower LOD in a wide linear range than the pristine UiO-66. This justifies the better transducing property of the electrode irradiated at this particular fluence. Thus, the study concludes that SHI irradiation can introduce structural modifications in the crystal structure of UiO-66 by inducing defects, which further helps to enhance the electroactive performance of the material. To obtain a larger sensitivity from such electrodes the transducer material can be modified by incorporating carrier enhancer like metal nanoparticle, conducting polymers, carbon compounds in the near future.

References

[1] Soni 1, S., Bajpai 2, P. K. & Arora 2, C. A review on metal-organic framework: synthesis, properties and application. *Characterization and Application of Nanomaterials*. **2**: 2018.

[2] Safaei, M. *et al.* A review on metal-organic frameworks: Synthesis and applications. *TrAC - Trends in Analytical Chemistry*. **118**: 401–425, 2019.

[3] Kirchon, A., Feng, L., Drake, H. F., Joseph, E. A. & Zhou, H.-C. From fundamentals to applications: a toolbox for robust and multifunctional MOF materials. *Chem Soc Rev*. **47**: 8611–8638, 2018.

[4] Han, Y. *et al.* Facile synthesis of morphology and size-controlled zirconium metal–organic framework UiO-66: the role of hydrofluoric acid in crystallization. *CrystEngComm*. **17**: 6434–6440, 2015.

[5] Zhang, Q. *et al.* Heteropoly acid-encapsulated metal–organic framework as a stable and highly efficient nanocatalyst for esterification reaction. *RSC Adv*. **9**: 16357–16365, 2019.

[6] Sholl, D. S. & Lively, R. P. Defects in Metal–Organic Frameworks: Challenge or Opportunity? *J Phys Chem Lett*. **6**: 3437–3444, 2015.

[7] Gutov, O. V., Hevia, M. G., Escudero-Adán, E. C. & Shafir, A. Metal–Organic Framework (MOF) Defects under Control: Insights into the Missing Linker Sites and Their Implication in the Reactivity of Zirconium-Based Frameworks. *Inorg Chem*. **54**: 8396–8400, 2015.

[8] Wang, C., Li, A. R. & Ma, Y. L. Phosphomolybdic acid niched in the metal-organic framework UiO-66 with defects: An efficient and stable catalyst for oxidative desulfurization. *Fuel Processing Technology*. **212**: 106629, 2021.

[9] Zhang, X., Shi, X., Chen, J., Yang, Y. & Lu, G. The preparation of defective UiO-66 metal organic framework using MOF-5 as structural modifier with high sorption capacity for gaseous toluene. *J Environ Chem Eng*. **7**: 103405, 2019.

[10] Abhirami, K. M. *et al.* Effect of SHI irradiation on the morphology of SnO2 thin film prepared by reactive thermal evaporation. in *Vacuum*. **90**: 39–43, 2013.

[11] Kumaravel, R. *et al.* Effect of swift heavy ion irradiation on structural, optical and electrical properties of Cd2SnO4 thin films. *Nucl Instrum Methods Phys Res B*. **268**: 2391–2394, 2010.

[12] Ingle, N. N. *et al.* Influence of swift heavy ion irradiation on sensing properties of nickel-(NRs-Ni3HHTP2) metal-organic framework. *Journal of Materials Science: Materials in Electronics*. **32**: 18657–18668, 2021.

[13] Dutta, R. & Kumar, A. 100 MeV O7+ ion irradiation induced electrochemical enhancement in NiBTC metal-organic framework based composite polymer electrolytes incorporated with ionic liquid. *Mater Res Express*. **6**: 085305, 2019.

[14] Sarmah, D. & Kumar, A. Ion beam modified molybdenum disulfide-reduced graphene oxide/ polypyrrole nanotubes ternary nanocomposite for hybrid supercapacitor electrode. *Electrochim Acta*. **312**: 392–410, 2019.

[15] Nath, A. K. & Kumar, A. Enhancement in electrochemical properties of ionic liquid-based nanocomposite polymer electrolytes by 100 MeV Si9+ swift heavy ion irradiation. *Ionics (Kiel)*. **20**: 1711–1721, 2014.

[16] Nath, A. K. & Kumar, A. 100MeV Si9+ swift heavy ion irradiation induced enhancement in electrochemical properties of electrolyte membrane composites based on ionic liquid-polymer-nanocomposite. *J Memb Sci*. **485**: 30–41, 2015.

[17] Kamarou, A., Wesch, W., Wendler, E., Undisz, A. & Rettenmayr, M. Swift heavy ion irradiation of InP: Thermal spike modeling of track formation. *Phys Rev B*. **73**: 184107, 2006.

[18] Yang, Q., Zhang, H.-Y., Wang, L., Zhang, Y. & Zhao, J. Ru/UiO-66 Catalyst for the Reduction of Nitroarenes and Tandem Reaction of Alcohol Oxidation/Knoevenagel Condensation. *ACS Omega*. **3**: 4199–4212, 2018.

[19] Dey, S. *et al.* Localized thermal spike driven morphology and electronic structure transformation in swift heavy ion irradiated TiO2nanorods. *Nanoscale Adv*. **4**: 241–249, 2022.

[20] Kumar, V. *et al.* High-energy 120 MeV Au9+ ion beam-induced modifications and evaluation of craters in surface morphology of SnO2 and TiO2 nanocomposite thin films. *Appl Nanosci*. **9**: 1265–1280, 2019.

[21] Ali, Y., Kumar, V., Sonkawade, R. G. & Dhaliwal, A. S. Effect of swift heavy ion beam irradiation on Au–polyaniline composite films. *Vacuum*. **90**: 59–64, 2013.

[22] Tan, K. *et al.* Defect Termination in the UiO-66 Family of Metal-Organic Frameworks: The Role of Water and Modulator. *J Am Chem Soc*. **143**: 6328–6332, 2021.

[23] Yost, B. T., Gibbons, B., Wilson, A., Morris, A. J. & McNeil, L. E. Vibrational spectroscopy investigation of defects in Zr- and Hf-UiO-66. *RSC Adv*. **12**: 22440–22447, 2022.

[24] Driscoll, D. M. *et al.* Characterization of Undercoordinated Zr Defect Sites in UiO-66 with Vibrational Spectroscopy of Adsorbed CO. *Journal of Physical Chemistry C*. **122**: 14582–14589, 2018.

[25] Atzori, C. *et al.* Effect of Benzoic Acid as a Modulator in the Structure of UiO-66: An Experimental and Computational Study. *The Journal of Physical Chemistry C*. **121**: 9312–9324, 2017.

[26] Abhirami, K. M., Matheswaran, P., Gokul, B., Sathyamoorthy, R. & Asokan, K. Structural and morphological properties of Ag ion irradiated SnO_2 thin films. *IOP Conf Ser Mater Sci Eng*. **73**: 012113, 2015.

[27] Sindhu, P., Ananthram, K. S., Jain, A., Tarafder, K. & Ballav, N. Charge-transfer interface of insulating metal-organic frameworks with metallic conduction. *Nat Commun*. **13**: 7665, 2022.

[28] Wang, W., Fan, X., Liu, J., Yan, C. & Zeng, C. Temperature-related reaction kinetics of the vanadium (IV)/ (V) redox couple in acidic solutions. *RSC Adv.* **4**: 32405–32411, 2014.

[29] Shrivastava, A. & Gupta, V. Methods for the determination of limit of detection and limit of quantitation of the analytical methods. *Chronicles of Young Scientists*. **2**: 21, 2011.